PAPER

Check for updates

Hierarchically self-assembled NiCo$_2$O$_4$ nanopins as a high-performance supercapacitor cathodic material: a morphology controlled study

Shahed Hassanpoor* and Farzaneh Aghely

In this study, 3D hierarchically self-assembled NiCo$_2$O$_4$ nanopins were synthesized by a morphology controlled hydrothermal method. Structure, morphology, and composition of the samples were investigated using FT-IR, XRD, EDS, and SEM methods. Electrochemical tests such as cyclic voltammetry (CV) and galvanostatic charge/discharge (GCD) studies were done in a three-electrode system with 1.0 M Na$_2$SO$_4$ solution as the electrolyte for the supercapacitive study of the samples on a carbon paste electrode for the first time. The results confirmed the high-performance supercapacitive behavior of the dense nanostructure and acceptable stability during the charge–discharge cycle. The specific capacitance for the dense self-organized nanopins was calculated using a galvanostatic charge/discharge experiment which gave 2168 F g^{-1} at a current density of 5 A g^{-1}.

1. Introduction

Increasing demand for high-efficiency, renewable energy sources has led to many studies of modern electrode materials for energy storage in devices such as batteries and supercapacitors (SC).[1] The major advantage of supercapacitors is their higher power densities than batteries and conventional dielectric capacitors. The efficiency of supercapacitors is strongly dependent on the materials used in the preparation of the electrodes. So a lot of research has been done in this area and it is still going on. Some of the metal oxide electrode materials used in supercapacitors are RuO$_2$, MnO$_2$, NiO, Ni(OH)$_2$, Fe$_3$O$_4$, Co(OH)$_2$, Co$_3$O$_4$.[2] Among these, metal oxides, appear to be attractive in terms of its high theoretical capacity, low toxicity, natural abundance, and environment friendliness.[3] The three main categories of supercapacitors are electrochemical double-layer capacitor (EDLC), pseudocapacitor, and hybrid type. The mechanism of EDLCs is the separation of the electrostatic charge from the electrolyte on the electrode surface. In contrast, the mechanism in pseudocapacitors is due to faradaic redox reaction in the internal structure and surface of the electrode material.[4] The NiCo$_2$O$_4$ has shown better electrical and mechanical properties than the single-component metal oxides Co$_3$O$_4$ and NiO.[5] The porous structure of NiCo$_2$O$_4$ is also one more appealing approach to overcome the volume changes and enhance capacity retention because of more electroactive sites for redox reactions.[6] There are many methods for the synthesis of NiCo$_2$O$_4$ such as sol–gel,[7,8] hydrothermal,[9,10] electrodeposition,[11] and microwave-assisted synthesis.[12] Among these methods, the hydrothermal method has received more attention due to its low cost, simplicity,

and ability to control particle size and morphology.[13] Nowadays, nanomaterials have received much attention in the field of energy storage due to their amazing properties such as high surface area and convenience of surface modification.[14] A hierarchical nanostructure consists of a community of self-assembled nano-sized or smaller units with a particular order. It provides a more effective level than 1D and 2D structures.[15,16] On the other hand, these structures are more resistant to structural damage because of changes in volume due to its internal connections.[17] There are some studies on the synthesis of hierarchical NiCo$_2$O$_4$ nanostructures with different morphology such as urchin,[18] pine,[19] and porous[20] by a change in synthesis conditions.

In the present work, 3D hierarchically self-assembled NiCo$_2$O$_4$ nanopins were synthesized by a morphology controlled hydrothermal method. The samples were successfully characterized using FT-IR, XRD, SEM, and EDX mapping methods. The CV, GCD, and EIS tests were used for capacitance study of the materials on the carbon past as substrate. According to the best of our knowledge, this is the first report of carbon past as a substrate for use in supercapacitors. The key benefits of carbon paste electrodes include: low cost, simple design, low background current, ability to introduce various modifiers during paste preparation, easy removal of electrode surface layer, low ohmic resistance, wide potential range.[21] The results confirmed the high-performance supercapacitive behavior of the dense self-organized nanopins modified electrode.

2. Materials and methods

2.1. Instrumentation

Electrochemical experiments were done in a cell of three electrodes with an Ag/AgCl (in saturated KCl) as a reference

Department of Nanotechnology, Faculty of Engineering, University of Guilan, Rasht, Iran. E-mail: Shahed_Hassanpoor110@yahoo.com; S_Hassanpoor@guilan.ac.ir

electrode and a Pt wire was used as an auxiliary electrode with a PGSTAT 302N instrument (Autolab, NOVA software equipped, the Netherlands). Crystallographic characterization of the material was done by XRD measurements with an STOE-STADI diffractometer (Germany, Cu Kα = 1.54 Å). Morphological analysis was done with a field emission scanning electron microscopy (TESCAN, VEGA3, Czech Republic). An ultrasonic bath (SIGMA SONIC, 4 L, 100 W, Iran) was applied to synthesize and the dispersion process. Fourier transform infrared spectra (FTIR) were done with an infrared spectrometer (Bruker, Alpha, KBr disk, Germany). The hydrothermal synthesis was done with a 70 mL Teflon-lined autoclave.

2.2. Chemicals and reagents

Graphite powder, $NiCl_2 \cdot 6H_2O$, $CoCl_2 \cdot 6H_2O$, HCl, urea, CTAB, Na_2SO_4, $K_4Fe(CN)_6$, KCl, and ethanol from Merck were used as received. Nafion (5 wt% in ethanol, Sigma Aldrich) was used for electrode preparation. Other salts and solvents were analytical grade and were purchased from Merck. Daily solutions were prepared with doubly distilled deionized water.

2.3. Synthesis of hierarchically self-assembled $NiCo_2O_4$ nanopins

In a typical procedure, 0.237 g $NiCl_2 \cdot 6H_2O$, 0.474 g $CoCl_2 \cdot 6H_2O$, and 0.72 g urea were added to 50 mL doubly distilled deionized water in a 100 mL beaker and stirred for 20 min. The obtained solution was transferred to a 75 mL Teflon-lined autoclave and sealed and heated at 180 °C for 6 h in an electric oven. After the hydrothermal treatment, a purple suspension was obtained. The purple precipitate was filtered and washed with 5.0 mL distilled water and ethanol twice alternatively after cooling down to room temperature. Then, the precipitate was dried at 80 °C for 3 h. It was then transferred to the furnace and stored at 300 °C for 3 hours for final calcination and convert to black $NiCo_2O_4$ nanoparticles powder. The powder was washed with 5 mL distilled water and ethanol twice alternatively for removal of residual impurity and then dried at 80 °C for 3 h. Dense hierarchically self-assembled $NiCo_2O_4$ nanopins (DHSANPs) have been synthesized in the same manner as above, except that 0.15 g CTAB was added in the first step of the hydrothermal process.

Urea is chosen as a forced-hydrolysis agent in this study as it is water-soluble in temperatures between 80 and 100 °C and gradually decomposed into NH_3 and CO_2.[22] Further NH_3 reacts with water to produce NH_4^+ and OH^-.[23] In the initial step, a large portion of the initial nanocrystallite with high surface energy tend to gather around the interface of CO_2 gas and water or of CTAB and water. These aggregates then grow and unstable hollow structures formed due to gas bubbles burst. Therefore, CTAB play the roles in generating the hollow structure, selective adsorption, occupied effect, and prevention of agglomeration.[24]

2.4. Electrochemical study

To make the carbon paste, 18 mg of the graphite powder with 45 μL of silicone oil was mixed and then heated on the hotplate with stirring by a spatula for 15 minutes at 60 °C. Then, the above past is filled in a homemade Teflon electrode cavity (3
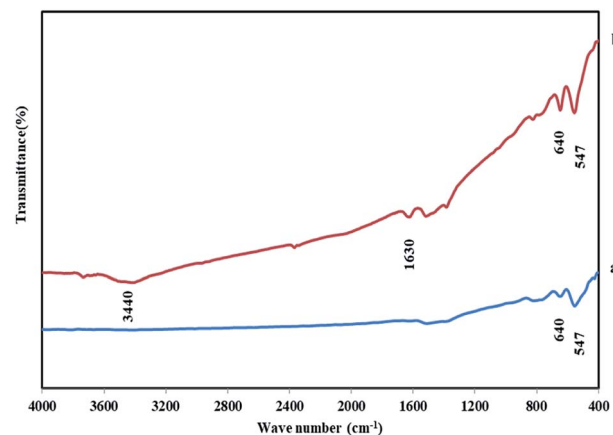

Fig. 1 The FT-IR spectrum of MHSANPs-$NiCo_2O_4$ (a) and DHSANPs-$NiCo_2O_4$ (b).

mm) by a spatula. A copper wire rod is attached to the sample from the back and pressed down. The electrode is then polished with a piece of paper to shine. It is then stored in an oven for 12 hours at 60 °C. The active material ink was prepared from 30 μL Nafion solution, 15 mg sample, and 3 mL ethanol. 3×5 μL of active material ink (equal to 72.2 μg of active material, loading mas, 1 mg cm^{-2}) was used to modify a freshly polished electrode by casting method after sonication for 10 min. The electrode dryness was done at 40 °C for 30 min. CV and GCD capacitor experiments were done in 1 M Na_2SO_4 solution as the electrolyte. EIS and CV study in 10 mM $K_4Fe(CN)_6$ and 0.1 M KCl also was investigate for the samples. The GCD study was applied to determine the capacitance performance of active materials. The specific capacitance (SC) in F g^{-1} dimensional was calculated from the following equation:

$$SC = \frac{I\Delta t}{m\Delta V}$$

where I, Δt, and ΔV are, the discharge current (A), the discharge time (s), and the discharge potential range (V), respectively, and
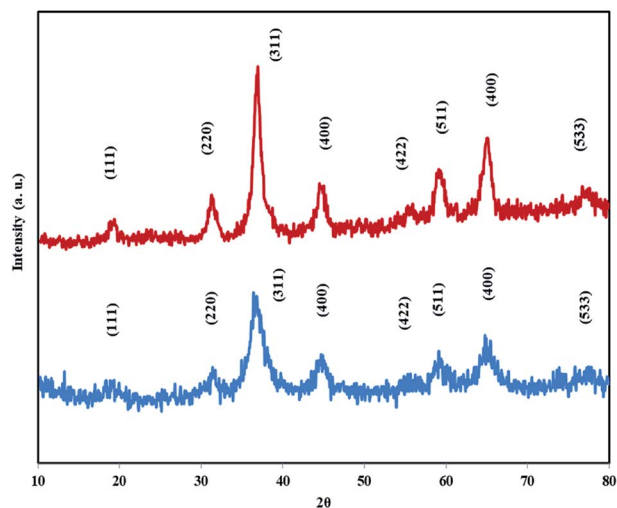

Fig. 2 The XRD patterns of MHSANPs-$NiCo_2O_4$ (a) and DHSANPs-$NiCo_2O_4$ (b).

the m (g) represents the mass of the active materials of the electrode.[25]

3. Results and discussion

3.1. Material characterizations

Material characterization was done with FT-IR, XRD, FE-SEM, and EDX methods. FT-IR spectroscopy is a convenient and efficient analysis for the characterization of a functionalized

nanoparticle and manufacturing bonds of nanoparticles. So, firstly the structure of $NiCo_2O_4$ nanostructures was characterized by FT-IR spectroscopy. Fig. 1 shows the FT-IR of $NiCo_2O_4$. The sharp bands at 547, 640 cm^{-1} are due to Ni–O and Co–O vibration at octahedral and tetrahedral sites respectively are shown in both samples.[26–28] The broad bands at 3440 and 1630 cm^{-1} are corresponding to the stretching and bending vibrations of the hydroxyl of the adsorbed water molecules.[29] For the DHSANPs sample, these peaks are wider, which can be
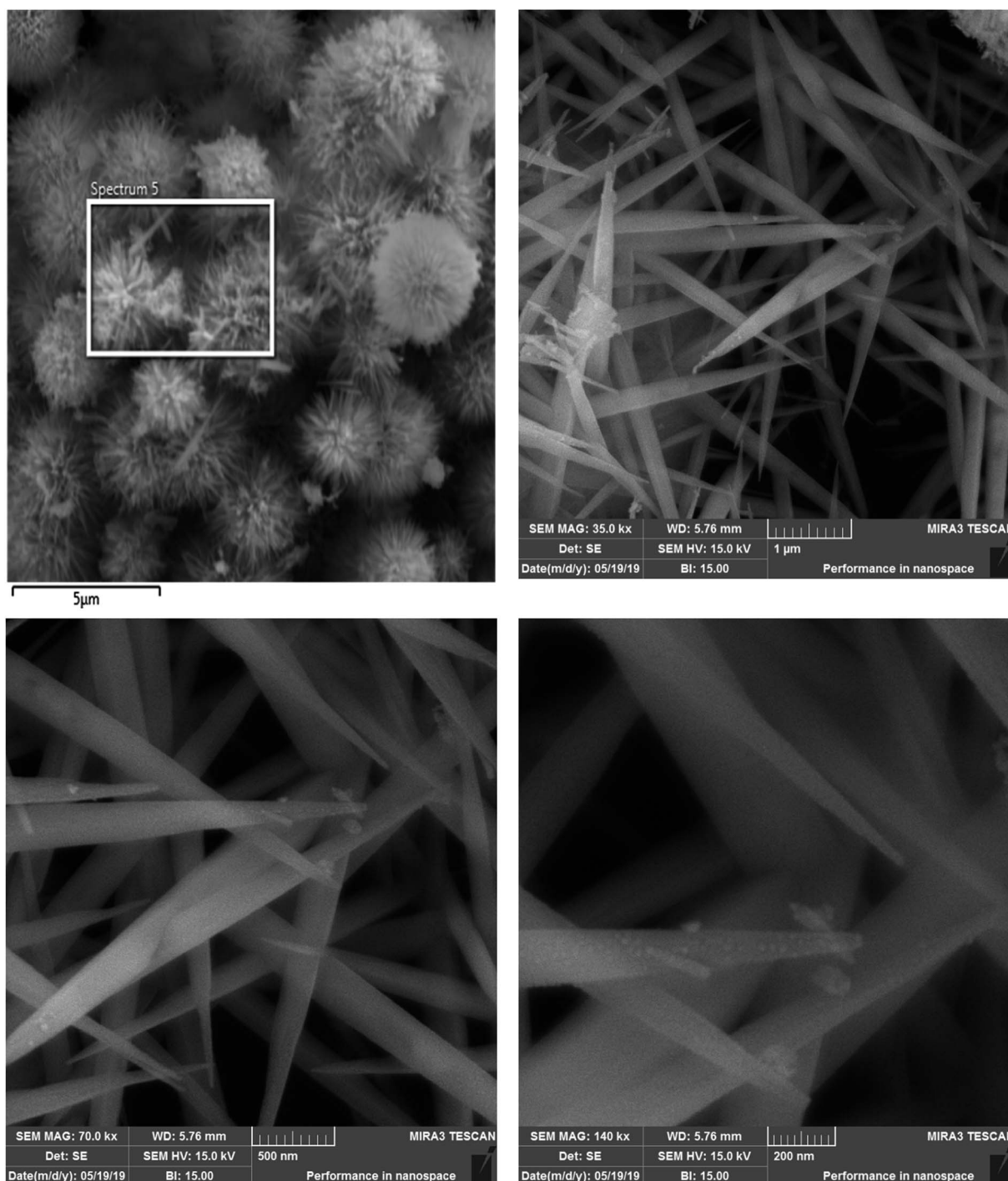

Fig. 3 FE-SEM of MHSANPs-$NiCo_2O_4$ in different scales.

due to the presence of many traps in its structure and adsorption of more water molecules.

X-ray diffraction analysis (XRD) is the most effective method for the structure and size of a crystalline nanoparticle. The XRD patterns of $NiCo_2O_4$ nanostructures are illustrated in Fig. 2. All the peaks in both samples correspond exactly to the spinel structure of $NiCo_2O_4$. The X-ray diffraction characteristic peaks at $2\theta = 18.9, 31.2, 36.7, 44.6, 55.4, 59.1, 64.9,$ and $77°$, which corresponding to plans of spinel $NiCo_2O_4$ (JCPDS no. 20-0781).[24–33] No peak is observed at other angles, indicating the purity of the synthesized material. The broad diffraction peaks reveal the small size of the products.

The estimated nanocrystallite size based on Scherrer's law from the (311) line also was done:[34]
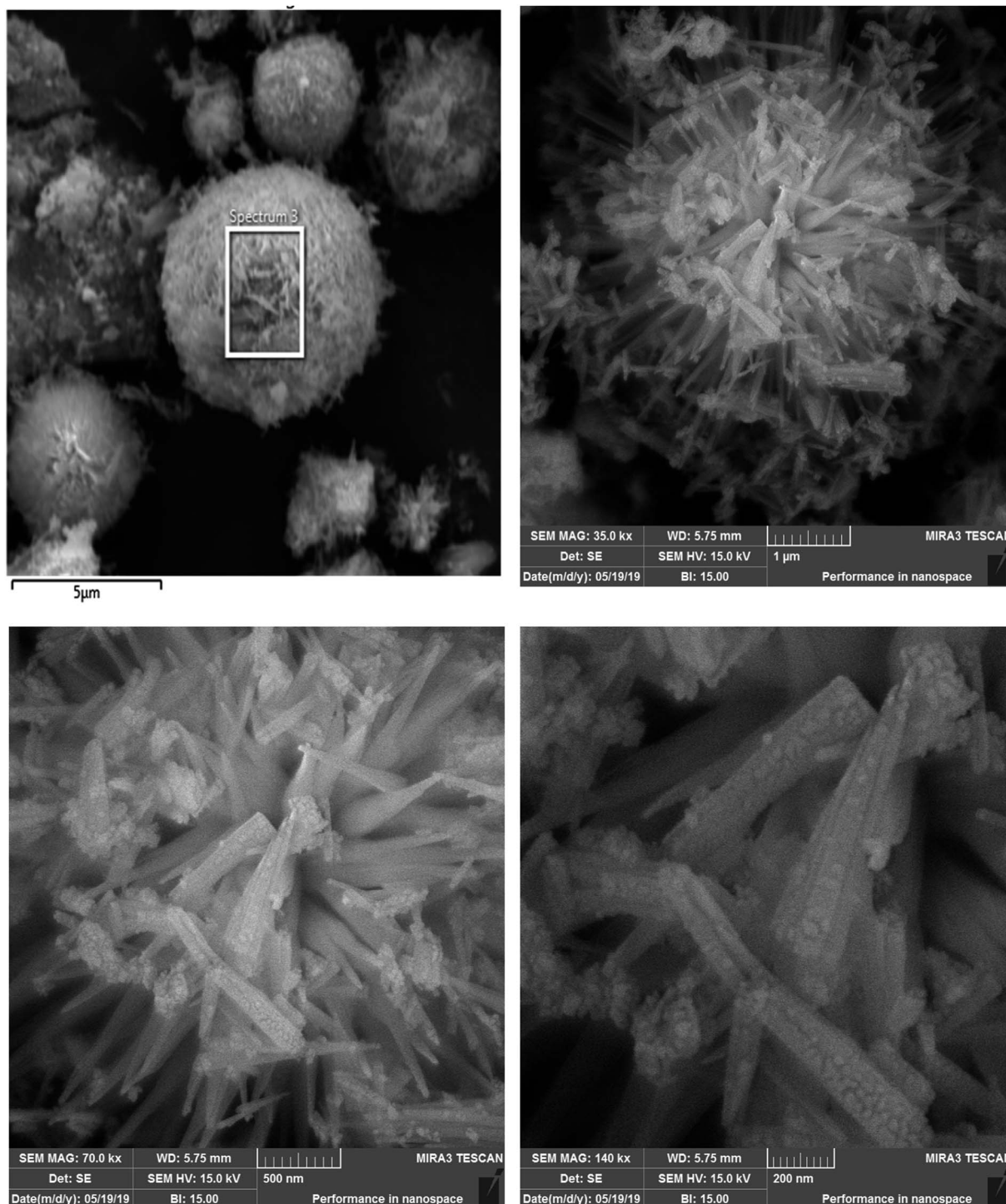

Fig. 4   FE-SEM of DHSANPs-$NiCo_2O_4$ in different scales.

$$d = 0.9\lambda/\beta_{1/2}\cos\theta$$

where λ is the wavelength of the X-ray source, $\beta_{1/2}$ is the half-height width of the diffraction peak (measured in radians) and θ is the diffraction angle was about 10 nm for both $NiCo_2O_4$ nanopins.

The morphological characterizations of the samples were done by FE-SEM. Fig. 3 shows surfactant-free monodispersed hierarchically self-assembled $NiCo_2O_4$ nanopins (MHSANPs) in different scales. Fig. 4 shows dense self-organized nanopins in different scales. Generally, the formation of hierarchical structures consists of five stages. The first stage is the nucleation. Secondly, the nuclei come together by a self-aggregating mechanism due to its high surface energy. Then the nanocrystals are formed. In the fourth stage, anisotropic growth is performed in pathways with optimal energy. In the end, Ostwald's process can be accomplished, and larger particles will be larger at the expense of smaller particles. This happens if the nuclei are in the supersaturated state for a longer time.[15,35] The CTAB presence, allows the nuclei to remain supersaturating due to the greater stability based on the interaction between surfactant and the nanoparticles and allowed the nanoparticles to aggregate much more and the structure becomes more compact.

The chemical composition of the hierarchical $NiCo_2O_4$ nanostructures has been analyzed using EDS (Fig. 5). Fig. 5a
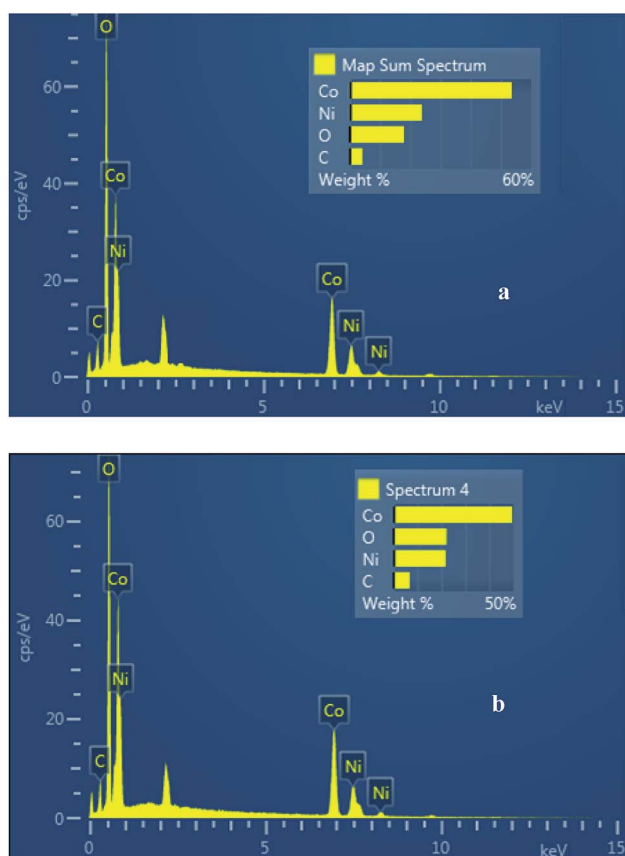
shows the EDS spectrum of surfactant-free MHSANPs-$NiCo_2O_4$. The wt% value for nickel (Ni, 23.85%), cobalt (Co, 52.36%) carbon (C, 4.24%) and oxygen (O, 19.56%) also are shown. Fig. 5b shows the EDS spectrum of DHSANPs-$NiCo_2O_4$. The wt% value for nickel (Ni, 21.75%), cobalt (Co, 49.41%) carbon (C, 6.75%) and oxygen (O, 22.09%) also are shown. As can be seen, the values with an acceptable approximation are close to the stoichiometric ratio in both nanostructures. The amount of carbon shown in both samples is low (about 4–6%) and is probably due to the residues of organic matter such as urea and CTAB, which in the case of surfactant used, the amount of carbon has been increased.

3.2. Electrochemical capacity study

The electrochemical capacitive studies of the materials and fabricated working electrodes are carried out as maintained in the general electrochemical procedure. The CVs were recorded in the −0.1 to 1.0 V potential window at different scan rates in the 1 M Na_2SO_4 electrolyte. Fig. 6a and b shows CV curves of MHSANPs-$NiCo_2O_4$ and DHSANPs-$NiCo_2O_4$ respectively at
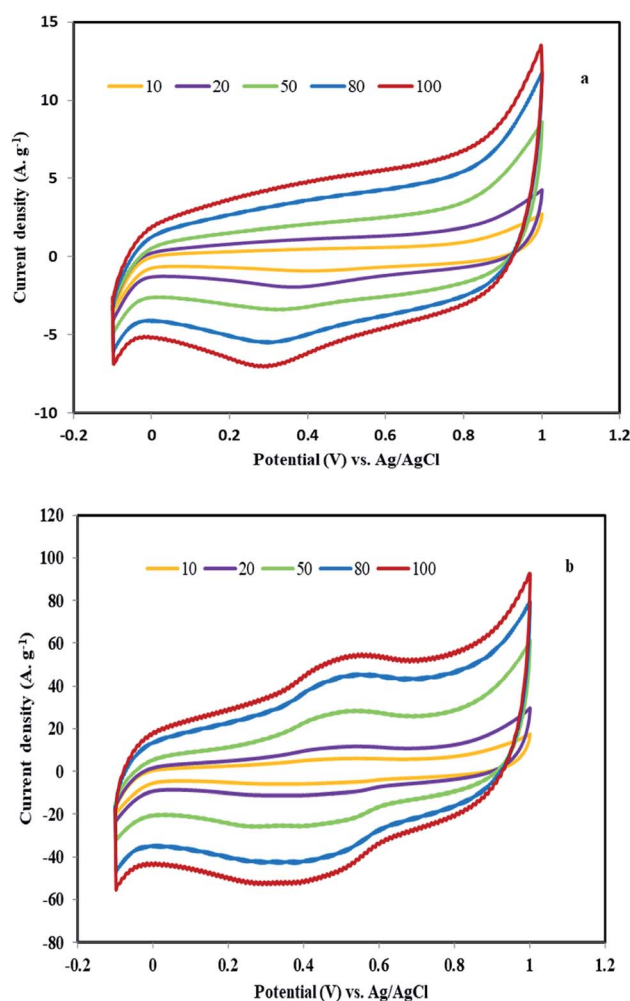

Fig. 5 EDS spectrum of MHSANPs-$NiCo_2O_4$ (a) and DHSANPs-$NiCo_2O_4$ (b) with its wt% of the elements.

Fig. 6 The CV curves of the MHSANPs-$NiCo_2O_4$ (a) and DHSANPs-$NiCo_2O_4$ (b) electrode at various scan rates ranged from 10 to 100 mV s^{-1} (b).
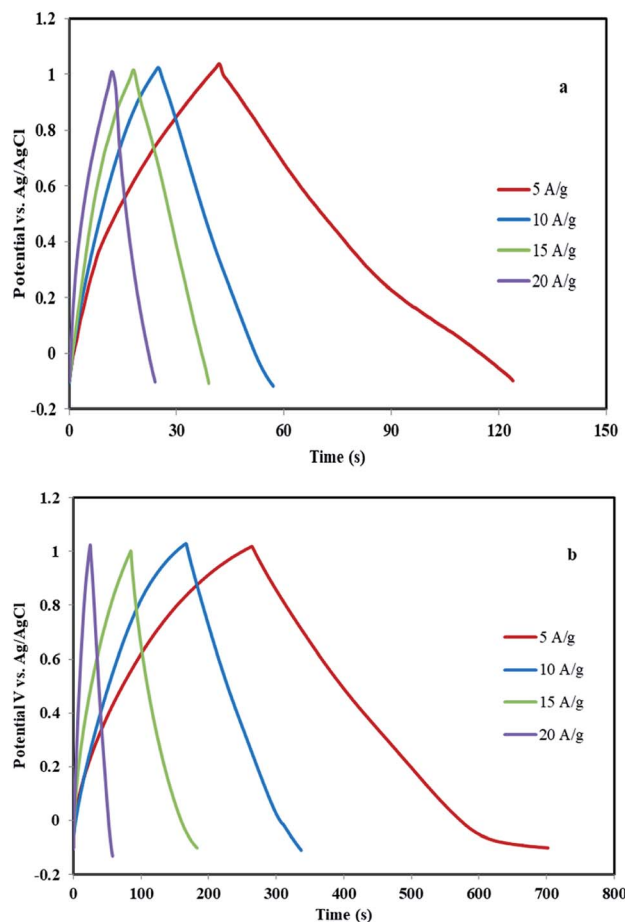
Fig. 7 The GCD curve of the MHSANPs-NiCo$_2$O$_4$ (a) and DHSANPs-NiCo$_2$O$_4$ (b) electrode with several current densities up to 20 A g^{-1}.

various scan rates ranging from 10 to 100 mV s^{-1}. The current peak at about 0.3 V and 0.5 V indicates the deintercalation and intercalation of the cation in the electrode and the electrochemical reversible redox reaction due to its faradic capacitance property can be seen.[36,37] The area of the CV of dense self-organized nanopins NiCo$_2$O$_4$ is significantly bigger than the other. This is probably due to its compact structure and the ability to store much more ions and thus its greater faradic capacitance. In other words, the ideal and symmetrical shape, especially for the dense nanostructure, is found throughout the potential window even at a low scanning rate, indicating its high capacity and low resistance. As the scanning rate increases, the current density increased but there are no tangible changes in the shape of the curve, indicating the stability of the material.[38,39]

To evaluate the real applicability of samples for supercapacitors, GCD tests were investigated at various current densities in the −0.1 to 1 V (vs. Ag/AgCl) potential window. Fig. 7a shows the GCD curve of the surfactant-free MHSANPs-NiCo$_2$O$_4$ with several current densities up to 20 A g^{-1}. The specific capacitances of this sample are thus calculated to be 377, 300, 288, and 218 F g^{-1} at a current density of 5, 10, 15, 20 A g^{-1}, respectively. Fig. 7b shows the GCD curve of the

DHSANPs-NiCo$_2$O$_4$ with several current densities up to 20 A g^{-1}. The specific capacitances of this sample are thus calculated to be 2168, 1650, 1363, and 618 F g^{-1} at a current density of 5, 10, 15, 20 A g^{-1}, respectively. As can be seen, the capacitance in the dense NiCo$_2$O$_4$ sample is about 6 times higher, probably due to its ability to ion storage and faradic redox. For both samples, the specific capacitance decreases steadily with increasing current density due to the lack of active material participating in the redox reaction and therefore voltage drop formation at high current density in both samples. Fig. 8a illustrates the relationship between the current density of the samples and the specific capacitance. As is evident, the specific capacitance of the dense self-organized nanopins NiCo$_2$O$_4$ is much higher in all cases. The cycling stability of the electrodes was obtained at 5 A g^{-1}, shows acceptable capacitance retention ratio which is above 95% and 97% for MHSANPs-NiCo$_2$O$_4$ and DHSANPs-NiCo$_2$O$_4$ respectively after 100 charge–discharge cycles (Fig. 8b).

The electron transfer capability of the electrode was studied with a CV of potassium ferrocyanide/ferricyanide redox reactions. For this reason, a solution of 10.0 mM K$_4$[Fe(CN)$_6$] and 0.10 M KCl was used as the electrolyte in the potential of −0.20 to +0.60 V. In this study, less difference between anodic and cathode peak potentials and greater current intensity confirming better rate of electron transfer and bigger active surface at electrode base of Randles–Sevcik equation. Fig. 9a shows cycling voltammograms of bare graphite electrode at various
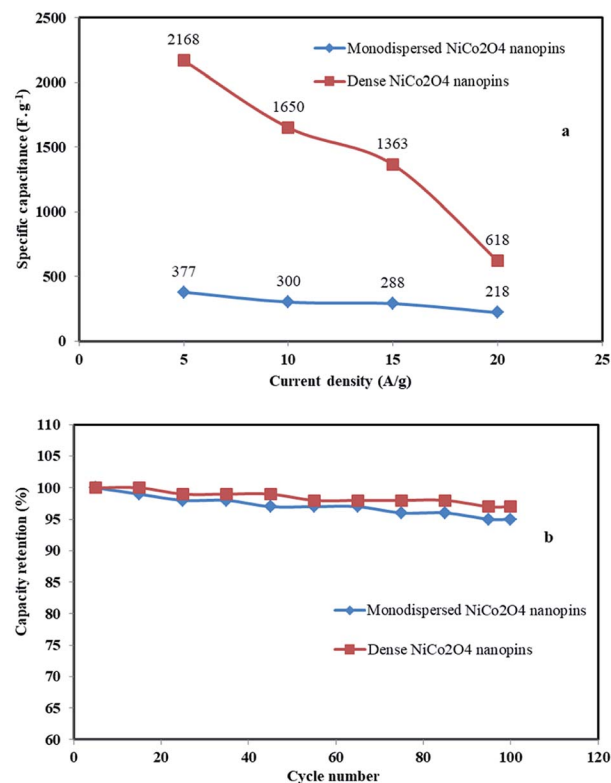

Fig. 8 The relationship between the current density of different materials and the specific capacitance (a) and the cycling stability of the electrodes was obtained at 5 A g^{-1} (b).
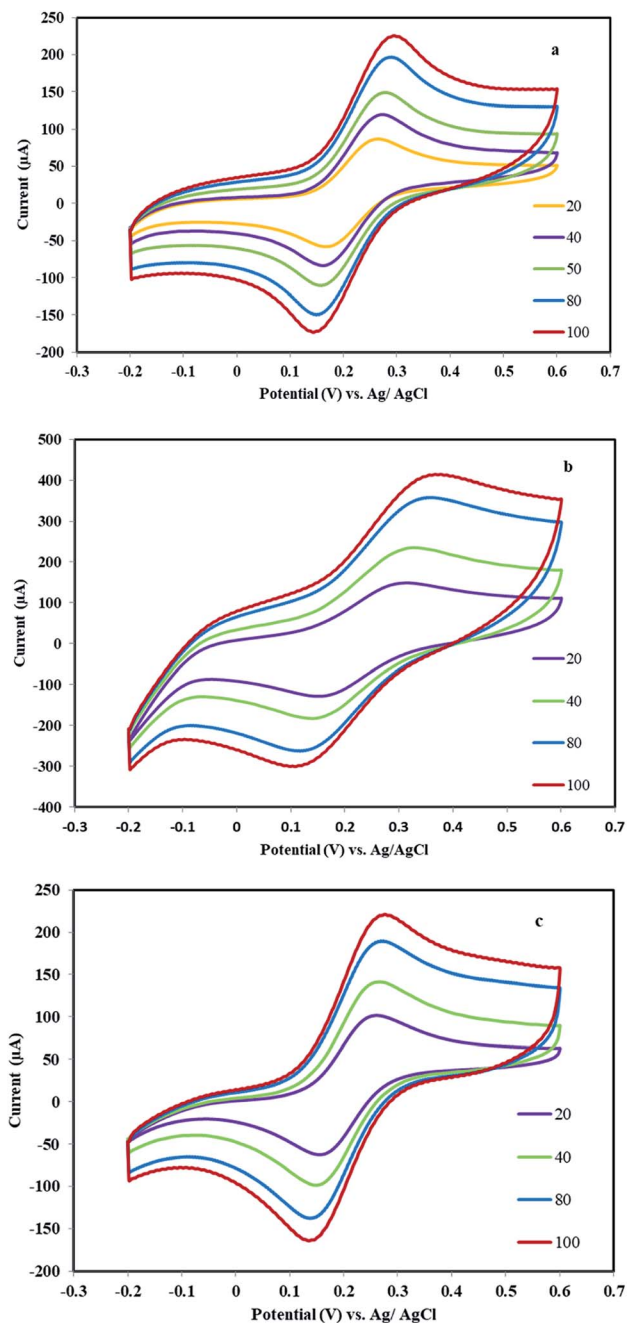
Fig. 9 Cycling voltammograms of a bare graphite electrode (a), MHSANPs-NiCo$_2$O$_4$ (b) and DHSANPs-NiCo$_2$O$_4$ (c) at various scan rates ranged from 20 to 100 mV s^{-1} electrode in 10 mM K$_4$Fe(CN)$_6$ containing 0.1 M KCl at different scan rates.

scan rates ranged from 20 to 100 mV s^{-1}. In this electrode, the diagram is slightly symmetrical ($\Delta E_p = 70$ mV for a scan rate of 40 mV s^{-1}) and the I_p reaches 223 µA at the rate of 100 mV s^{-1}. By modifying the electrode with the MHSANPs-NiCo$_2$O$_4$, the shape was changed and the intensity of the I_p reaches 408 µA ($\Delta E_p = 150$ mV for a scan rate of 40 mV s^{-1}), indicating a much better electron exchange in this sample (Fig. 9b). This could be due to the presence of separate nanopins and the higher ability to electron exchange at their tips. In the case of the DHSANPs-

NiCo$_2$O$_4$ dense self-organized nanopins NiCo$_2$O$_4$ electrode, it becomes more symmetrical and resembles the graphite state, which may be due to its compact state with a I_p of 218 µA at the rate of 100 mV s^{-1} ($\Delta E_p = 100$ mV for a scan rate of 40 mV s^{-1}) (Fig. 9c). As can be seen, it has a low difference between anodic and cathode peak potentials indicating acceptable reversibility and confirmed suitability of this electrode material for use in the supercapacitor. In all samples, by increasing the scan rate (v) from 20 to 100 mV s^{-1}, the peak current and peak separation potential increase with a gentle slope. As shown in Fig. 10, the redox peak currents were proportional to the square root of the scan rate for all samples, suggesting a diffusion-controlled process.[40–42]

EIS was used as a very useful technique for studying the interface between electrode and electrolyte. Therefore EIS experiments were done in a solution of 10.0 mM K$_4$[Fe(CN)$_6$]
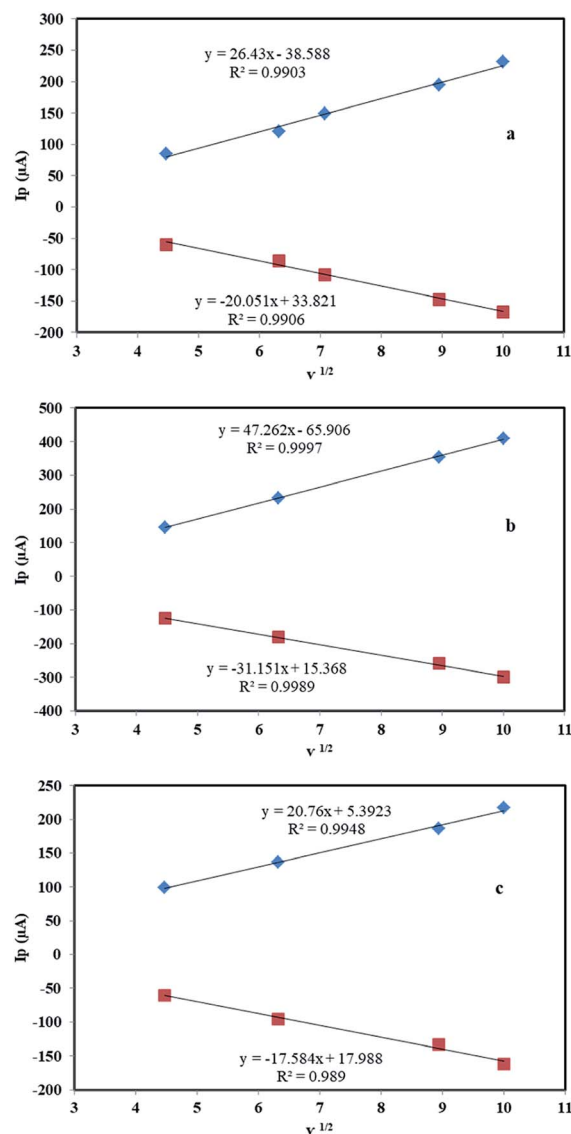

Fig. 10 The linear relationship between the redox peak currents and the square root of the scan rate of a bare graphite electrode (a), MHSANPs-NiCo$_2$O$_4$ (b) and DHSANPs-NiCo$_2$O$_4$ (c).
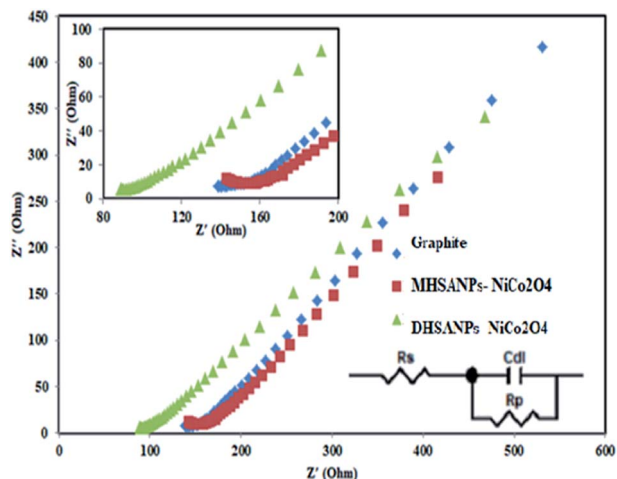
Fig. 11 Nyquist plots of EIS analysis of bare graphite electrode, MHSANPs-NiCo$_2$O$_4$ and DHSANPs-NiCo$_2$O$_4$ in 10 mM K$_4$Fe(CN)$_6$ containing 0.1 M KCl and the equivalent circuit model.

and 0.10 M KCl at OCP with an AC perturbation of 5 mV in the frequency range of 0.1 Hz to 100 kHz. The equivalent circuit consists of R_s, C_{dl}, and R_p (Fig. 11). R_s is internal resistance is a component of the supercapacitor cell and in the Nyquist plot is the intercept value at the horizontal axis. R_p is the summation of R_{ct} as a semicircle at high frequency due to kinetic control and R_W (Warburg impedance) as a straight line at low frequency due to mass transport control. C_{dl} is the capacitance of the double layer.[43] The data for all electrodes were fitted with the Zview (version 3.5d) software. The values of R_p for the electrodes were as follows: bare graphite (281 ohm), modified with MHSANPs-NiCo$_2$O$_4$ (182 ohm) and modified with DHSANPs-NiCo$_2$O$_4$ (237 ohm), show low electron resistance for electrodes as an important property in supercapacitor application. The lowest resistance in the MHSANPs-NiCo$_2$O$_4$ sample is due to the needle heads like pins and the fast electron transfer from them. These results strongly confirm the ferrocyanide/ferricyanide redox study results.

Table 1 Comparison of characteristic performance by the developed method with different NiCo$_2$O$_4$ based electrode materials[a]

Active material	Precursors, time and temperature	Morphology	Average size (nm)	Synthesis method	Electrolyte	Substrate	Capacity (F g^{-1})	Ref.
NiCo$_2$O$_4$	Co(Ac)$_2$·4H$_2$O, Ni(Ac)$_2$·4H$_2$O, 3 h, 400 °C	Coral like nanoparticle	170	Sol–gel	KOH 1 M	Ni foam	217	7
NiCo$_2$O$_4$/meso carbon	Ni(NO$_3$)$_2$·6H$_2$O, Co(NO$_3$)$_2$·6H$_2$O, urea, 8 h, 95 °C	Nanoneedles	50	Hydrothermal	KOH 3 M	Ni foam	458	26
NiCo$_2$O$_4$	NiCl$_2$·6H$_2$O, CoCl$_2$·6H$_2$O, urea, 6 h, 120 °C	Urchin like nanostructures	150	Hydrothermal	KOH 3 M	Ni foam	1348	18
NiCo$_2$O$_4$	Co(Ac)$_2$·4H$_2$O, Ni(Ac)$_2$·4H$_2$O, CTAB, NaHCO$_3$, 6 h, 35 °C	Hollow urchin	15	Sol–gel	KOH 6 M	Ni foam	95	24
NiCo$_2$O$_4$	Co(Ac)$_2$·4H$_2$O, Ni(Ac)$_2$·4H$_2$O, urea, 5.5 h, 150 °C	Nanorods	25	Solvothermal	KOH 2 M	Ni foam	600	22
GO/MWCNT/ NiCo$_2$O$_4$	Ni(NO$_3$)$_2$·6H$_2$O, Co(NO$_3$)$_2$·6H$_2$O, urea, 8 h, 90 °C	Nanoparticles	15	Sol–gel	KOH 6 M	Stainless-steel	707	44
NiCo$_2$O$_4$/RGO	Ni(NO$_3$)$_2$·6H$_2$O, Co(NO$_3$)$_2$·6H$_2$O, NH$_3$, 12 h, 60 °C	Nanoparticles	—	Sol–gel	KOH 6 M	Ni foam	835	45
NiCo$_2$O$_4$	Ni(NO$_3$)$_2$·6H$_2$O, Co(NO$_3$)$_2$·6H$_2$O, NH$_4$F, urea, 5 h, 100 °C	3D hierarchical nanosheet–nanowire cluster (pine-like)	75	Sol–gel	KOH 2 M	Ni foam	2000	19
NiCo$_2$O$_4$-CNT@DNA	Ni(NO$_3$)$_2$·6H$_2$O, Co(NO$_3$)$_2$·6H$_2$O, HMTA, DNA, 5 h, 90 °C	Nanoparticle	8	Sol–gel	KOH 3 M	Ni foam	760	46
NiCo$_2$O$_4$	Ni(NO$_3$)$_2$·6H$_2$O, Co(NO$_3$)$_2$·6H$_2$O, EDTA, PEI, 1 h, 500 °C	3D hierarchical porous network-like	27	Sol–gel	KOH 3 M	Ni foam	587	20
NiCo$_2$O$_4$	NiCl$_2$·6H$_2$O, CoCl$_2$·6H$_2$O, urea, 6 h, 180 °C	Monodisperse hierarchically self-assembled nanopins	10	Hydrothermal	Na$_2$SO$_4$ 1 M	Carbon past	377	This work
NiCo$_2$O$_4$	NiCl$_2$·6H$_2$O, CoCl$_2$·6H$_2$O, urea, CTAB, 6 h, 180 °C	Dense hierarchically self-assembled nanopins	10	Hydrothermal	Na$_2$SO$_4$ 1 M	Carbon past	2168	This work

[a] Ethylenediaminetetraacetic acid (EDTA), polyethyleneimine (PEI), hexamethylenetetramine (HMTA), deoxyribonucleic acid (DNA), carbon nanotube (CNT).

4. Conclusions

In the present work, a morphology controlled hydrothermal method for the synthesis of 3D hierarchically self-assembled $NiCo_2O_4$ nanopins was synthesized. By the developed method two monodisperse and dense nanopins structures were produced and successfully characterized with proper methods. The CV, GCD, and EIS tests were used for capacitance study of the materials. The dense self-organized nanopins delivered the highest specific capacitance of 2168 F g^{-1} at 5 A g^{-1} current density, with the capacity retention as high as 97% after 100 cycles. Characteristic performance by the developed method was compared with different $NiCo_2O_4$ based electrode materials. The results are shown in Table 1. As can be seen, the present study shows a straightforward synthesis procedure for the synthesis of 3D hierarchically $NiCo_2O_4$ nanopins and acceptable electrochemical performance. According to the best of our knowledge, this is the first report of carbon past as a substrate for use in supercapacitors. Because of the mentioned reasons, ensure that such material can be applied as cathodic electrode material in energy storage devices and large scale commercial applications.

Conflicts of interest

There are no conflicts to declare.

References

1 A. S. Aricò, P. Bruce, B. Scrosati, J.-M. Tarascon and W. v. Schalkwijk, *Nat. Mater.*, 2005, **4**, 366–377.
2 P. C. Chen, G. Shen, Y. Shi, H. Chen and C. Zhou, *ACS Nano*, 2010, **4**, 4403–4411.
3 A. K. Mondal, D. Su, S. Chen, X. Xie and G. Wang, *ACS Appl. Mater. Interfaces*, 2014, **6**, 14827–14835.
4 M. vengari, T. Pryor and L. Jiang, *J. Energy Eng.*, 2013, **139**, 72–79.
5 F. Fu, J. Li, Y. Yao, X. Qin, Y. Dou, H. Wang, J. Tsui, K. Chan and M. Shao, *ACS Appl. Mater. Interfaces*, 2017, **9**, 16194–16201.
6 J. Xu, L. He, W. Xu, H. Tang, H. Liu, T. Han, Y. Zhang and C. Zhang, *Electrochim. Acta*, 2014, **145**, 185–192.
7 Y. Q. Wu, X. Y. Chen, P. T. Ji and Q. Q. Zhou, *Electrochim. Acta*, 2011, **56**, 7517–7522.
8 Y. Zhang, Y. Ru, H.-L. Gao, S.-W. Wang, J. Yan, K.-Z. Gao, X.-D. Jia, H.-W. Luo, H. Fang, A.-Q. Zhang and L.-Z. Wang, *J. Electrochem. Sci. Eng.*, 2019, **9**, 243–253.
9 C. Wang, E. Zhou, X. Deng, M. Shao, J. Huang, X. Wei and X. Xu, *Sci. Adv. Mater.*, 2016, **8**, 1298–1304.
10 M. Chatterjee, S. Saha, S. Das and S. K. Pradhan, *J. Alloys Compd.*, 2020, **821**, 153503.
11 J. Du, G. Zhou, H. Zhang, C. Cheng, J. Ma, W. Wei, L. Chen and T. Wang, *ACS Appl. Mater. Interfaces*, 2013, **5**, 7405–7409.
12 D. Carriazo, J. Patino, M. C. Gutiérrez, M. L. Ferrer and F. d. Monte, *RSC Adv.*, 2013, **3**, 13690–13695.
13 C. Wang, E. Zhou, W. He, X. Deng, J. Huang, M. Ding, X. Wei, X. Liu and X. Xu, *Nanomaterials*, 2017, **7**, 1–23.
14 S. Hassanpoor, G. Khayatian and A. R. J. Azar, *Microchim. Acta*, 2015, **182**, 1957–1965.
15 M. Fang, G. Dong, R. Wei and J. C. Ho, *Adv. Energy Mater.*, 2017, **7**, 1700559–1700584.
16 Z. Ren, Y. Guo, C.-H. Liu and P.-X. Gao, *Front. Chem.*, 2013, **1**, 1–22.
17 X. Liu, S. Shi, Q. Xiong, L. Li, Y. Zhang, H. Tang, C. Gu, X. Wang and J. Tu, *ACS Appl. Mater. Interfaces*, 2013, **17**, 8790–8795.
18 Q. Wang, B. Liu, X. Wang, S. Ran, L. Wang, D. Chen and G. Shen, *J. Mater. Chem.*, 2012, **22**, 21647–21653.
19 Y. Chen, B. Qu, L. Hu, Z. Xu, Q. Li and T. Wang, *Nanoscale*, 2013, **5**, 9812–9820.
20 C. z. Yuan, J. Li, L. n. Hou, J. Lin, X. g. Zhang and S. Xiong, *J. Mater. Chem. A*, 2013, **1**, 11145–11151.
21 K. Vytras, I. Švacara and R. Metelka, *J. Serb. Chem. Soc.*, 2009, **74**, 1021–1033.
22 E. Jokar, A. I. zad and S. Shahrokhian, *J. Solid State Electrochem.*, 2015, **19**, 269–274.
23 D. Guragain, C. Z. equine, T. Poudel, D. N. eupane, R. K. Gupta and S. R. Mishra, *J. Nanosci. Nanotechnol.*, 2020, **20**, 2526–2537.
24 Y. Lei, Y. Wang, W. Yang, H. Yuan and D. Xiao, *RSC Adv.*, 2015, **5**, 7575–7583.
25 S. Zhang and N. Pan, *Adv. Energy Mater.*, 2014, **1401401**, 2–19.
26 Y. Zhang, Y. Zhang, D. Zhang and L. Sun, *Dalton Trans.*, 2017, **46**, 9457–9465.
27 H. Zhang, H. Li, H. Wang, K. He, S. Wang, Y. Tang and J. Chen, *J. Power Sources*, 2015, **280**, 640–648.
28 K. Pandi, M. Sivakumar, S.-M. Chen, Y.-H. Cheng and T.-W. Chen, *Int. J. Electrochem. Sci.*, 2018, **13**, 1227–1240.
29 S. Liu, C. h. An, X. y. Chang, H. Guo, L. Zang, Y. Wang, H. Yuan and L. Jiao, *J. Mater. Sci.*, 2018, **54**, 2658–2668.
30 A. K. Das, R. K. Layek, N. H. Kim, D. Jung and J. H. Lee, *Nanoscale*, 2014, **6**, 10657–10665.
31 L. J. Cardenas-Flechas, A. M. Raba and M. Rincón-Joya, *Dyna*, 2020, **87**, 184–191.
32 J.-C. Xing, Y.-L. Zhu and Q.-J. Jiao, *J. New Mater. Electrochem. Syst.*, 2014, **17**, 209–211.
33 G. D. Park, Y. N. Ko and Y. C. Kang, *Sci. Rep.*, 2014, **4**, 1–7.
34 M. H. Alfaruqi, S. Islam, J. Gim, J. Song, S. Kim, D. Pham, J. Jo, Z. Xiu, V. Mathew and J. Kim, *Chem. Phys. Lett.*, 2016, **650**, 64–68.
35 S. K. Kulkarni, *Nanotechnology: Principles and Practices*, Springer International Publishing, 2015.
36 T. Brousse, D. Bélanger and J. W. Long, *J. Electrochem. Soc.*, 2015, **162**, A5185–A5189.
37 X. Wang, Y. Fang, B. Shi, F. Huang, F. Rong and R. Que, *Chem. Eng. J.*, 2018, **344**, 311–319.
38 A. k. Mondel, B. Wang, D. Su, Y. Wang, S. Chen, X. Zhang and G. Wang, *Mater. Chem. Phys.*, 2014, **143**, 740–746.
39 T. K. Das, S. Banerjee, A. Kumar, A. K. Debnath and V. Sudarsan, *Solid State Sci.*, 2019, **96**, 105952.
40 M. M. Rahman and I. C. Jeon, *J. Braz. Chem. Soc.*, 2007, **18**, 1150–1157.
41 X. Chen, L. Ji, Y. Zhou and K. Wu, *Sci. Rep.*, 2016, **26044**, 1–9.

42 S. Hassanpoor and N. Rouhi, *Int. J. Environ. Anal. Chem.*, 2019, DOI: 10.1080/03067319.2019.1669582.

43 H. Tan and Z. Ren, *Mater. Sci. Forum*, 2016, **14**, 14–21.

44 S. Ramesh, D. Vikraman, H.-S. Kim, H. S. Kim and J.-H. Kim, *J. Alloys Compd.*, 2018, **765**, 369–379.

45 H. W. Wang, Z. A. Hu, Y. Q. Chang, Y. L. Chen, H. Y. Wu, Z. Y. Zhang and Y. Y. Yang, *J. Mater. Chem.*, 2011, **21**, 10504–10511.

46 Y. Xue, T. Chen, S. Song, P. Kim and J. Bae, *Nano Energy*, 2019, **56**, 751–758.